

Euler fluid in two dimensions: Statistical approach

Calvin A. F. Farias , Renato Pakter , and Yan Levin 

Instituto de Física, UFRGS, Porto Alegre, Rio Grande do Sul 91501-970, Brazil



(Received 2 November 2022; accepted 19 January 2023; published 10 February 2023)

We use Kirchhoff's vortex formulation of 2D Euler fluid equations to explore the equilibrium state to which a 2D incompressible fluid relaxes from an arbitrary initial flow. The vortex dynamics obeys Hamilton's equations of motion with x and y coordinates of the vortex position forming a conjugate pair. A state of fluid can, therefore, be expressed in terms of an infinite number of infinitesimal vortices. If the vortex dynamics is mixing, the final equilibrium state of the fluid should correspond to the maximum of Boltzmann entropy, with the constraint that all the Casimir invariants of the fluid must be preserved. This is the fundamental assumption of Lynden-Bell's theory of collisionless relaxation. In this paper, we will present a Monte Carlo method which allows us to find the maximum entropy state of the fluid starting from an arbitrary initial condition. We will then compare this prediction with the results of molecular dynamics simulation and demonstrate that the final state to which the fluid evolves is, actually, very different from that corresponding to the maximum of entropy. This indicates that the mixing assumption is not correct. We will then present a different approach based on core-halo distribution which allows us to accurately predict the final state to which the fluid will relax, starting from an arbitrary initial condition.

DOI: [10.1103/PhysRevE.107.024115](https://doi.org/10.1103/PhysRevE.107.024115)

I. INTRODUCTION

Dynamics of inviscid 2D fluids has a long history. The fluid equations of motion were written by Euler and studied in great detail by Kirchhoff and others. Of particular interest are large vortex structures to which sheared 2D fluids are observed to evolve. The giant vortices, such as Jupiter's Red Spot are of great importance in atmospheric science. To explain the formation of these large-scale structures, Onsager appealed to statistical mechanics [1]. In particular, he showed that if one treats vortices as particles and invokes Boltzmann's statistical mechanics, the maximum entropy state will have negative absolute temperature. The reason for such a population-inverted state is that, at variance with particle systems, for fluid confined within a finite area—such as a planetary surface—the accessible phase space has finite volume. The compact phase space will result in entropy having two branches, one in which it increases with energy similar to normal particle systems, and a branch in which entropy decreases with energy. This second branch will lead to negative absolute temperature, if one applies the usual rules of thermodynamics to define temperature. The existence of a negative temperature state would lead to a population inversion in which microscopic vortices bunch together, resulting in a giant vortex. In practice, one does not need to have fluid confined in finite space to meet the conditions for the existence of a negative temperature state—conservation of angular momentum results in an effective confining potential, which also leads to self-confinement and population inversion [2].

One problem with Onsager's approach is that it uses classical statistical mechanics to treat microscopic vortices inside Euler fluid. Indeed, one can write 2D Euler equations [3] in terms of vortex density $\Gamma(\mathbf{r}, t) = (\nabla \times \mathbf{u}(\mathbf{r}, t)) \cdot \hat{\mathbf{k}}$, where \mathbf{u}

is the fluid velocity, $\hat{\mathbf{k}}$ is a unit normal to the fluid plane, and $\mathbf{r} \equiv x\hat{\mathbf{i}} + y\hat{\mathbf{j}}$. The motion of the vortex density is then governed by

$$\frac{\partial \Gamma}{\partial t} + (\mathbf{u} \cdot \nabla) \Gamma = 0, \quad (1)$$

$$\nabla \cdot \mathbf{u} = 0. \quad (2)$$

The incompressibility condition for \mathbf{u} allows us to introduce a stream function ψ , such that $\mathbf{u}(\mathbf{r}, t) = \nabla \times \psi(\mathbf{r}, t)\hat{\mathbf{k}}$, which using the definition of vortex density then satisfies the Poisson equation

$$\Delta \psi(\mathbf{r}, t) = -\Gamma(\mathbf{r}, t), \quad (3)$$

the solution to which can be written in terms of a Green's function, which in open space takes the form $G(\mathbf{r}_i, \mathbf{r}_j) = (-1/2\pi) \ln |\mathbf{r}_i - \mathbf{r}_j|$,

$$\psi(\mathbf{r}, t) = \int \Gamma(\mathbf{r}', t) G(\mathbf{r}, \mathbf{r}') d\mathbf{r}', \quad (4)$$

$$= -\frac{1}{2\pi} \int \Gamma(\mathbf{r}', t) \ln |\mathbf{r} - \mathbf{r}'| d\mathbf{r}'. \quad (5)$$

The vortex density can be written in terms of individual vorticity of point vortices, $\Gamma(\mathbf{r}, t) = \sum_i \Gamma_i \delta(\mathbf{r} - \mathbf{r}_i(t))$. Since the velocity of point vortices must be the same as of fluid at the same location, we conclude that $\dot{\mathbf{r}}_i = \nabla_i \times \sum_{j \neq i} \Gamma_j G(\mathbf{r}_i, \mathbf{r}_j) \hat{\mathbf{k}}$ and we see that the vortex dynamics has a Hamilton-like structure,

$$\Gamma_i \dot{x}_i = \frac{\partial \mathcal{H}}{\partial y_i}, \quad \Gamma_i \dot{y}_i = -\frac{\partial \mathcal{H}}{\partial x_i}, \quad i \in \{1, 2, \dots, N\}, \quad (6)$$

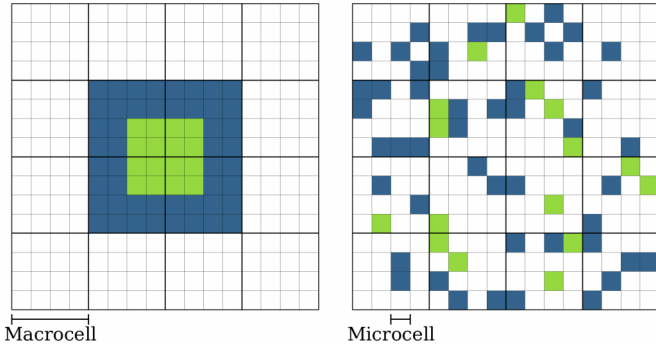


FIG. 1. Phase-space evolution of the density levels: The left panel shows the initial condition of a two-level distribution function and the right panel shows an intermediary state at some later time.

where we have defined the Kirchhoff function as

$$\mathcal{H} = \frac{1}{2} \sum_{i,j} \Gamma_i \Gamma_j G(\mathbf{r}_i, \mathbf{r}_j), \quad (7)$$

$$= -\frac{1}{4\pi} \sum_{i,j} \Gamma_i \Gamma_j \ln |\mathbf{r}_i - \mathbf{r}_j|. \quad (8)$$

A fundamental theorem of fluid dynamics [4,5] states that any smooth solution of a 2D Euler equation can be approximated over a finite time interval using N point vortices of vanishing vorticity $\Gamma_i \sim \pm 1/N$ in the limit $N \rightarrow \infty$. This corresponds precisely to the thermodynamic limit for systems with long-range interactions [6–8]. It is well-known that in the limit $N \rightarrow \infty$, such systems do not relax to thermodynamic equilibrium, precluding direct application of Boltzmann-Gibbs statistical mechanics. This invalidates Onsager’s attempt to apply standard statistical mechanics arguments to explain the formation of large structures in 2D Euler fluids.

In this paper, we will restrict our attention to flows with circulation of only one sign, however, the theoretical discussion presented below can be easily extended to arbitrary flows containing both clockwise and counterclockwise vortices. If all vortices have the same vorticity $\Gamma_i = \Gamma_T/N$, where Γ_T is the total vorticity, the vortex equations of motion can be further simplified to read

$$\frac{dx_i}{dt} = \frac{\partial \psi}{\partial y}, \quad \frac{dy_i}{dt} = -\frac{\partial \psi}{\partial x}. \quad (9)$$

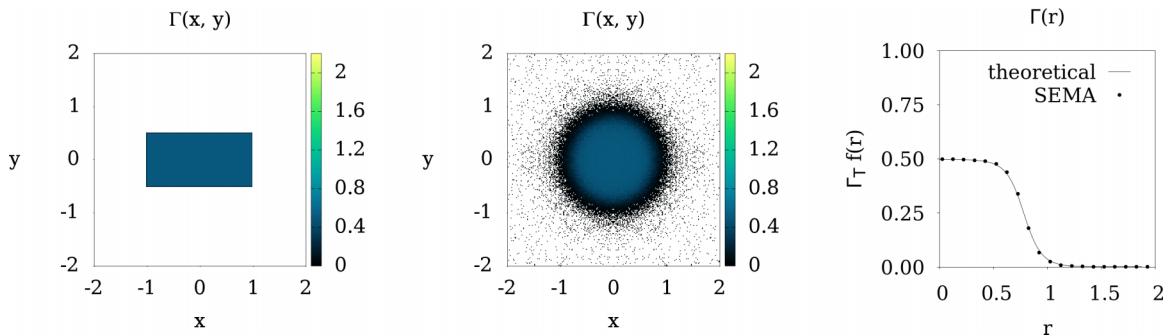


FIG. 2. Snapshots of the phase space obtained using the SEMA. The left panel shows the initial condition of a one-level distribution function, $f(x, y) = 0.5 \Theta(1.0 - |x|) \Theta(0.5 - |y|)$, normalized to unity. The central panel shows the steady state corresponding to LB equilibrium, while the right panel shows the radial distribution.

Defining the vortex distribution function $f(\mathbf{r}, t)$, the vortex density can be written as $\Gamma(\mathbf{r}, t) \equiv \Gamma_T f(\mathbf{r}, t)$, where we have normalized the distribution function to unity. Since the vortices are simply advected by the flow, as per Eq. (1), the distribution function satisfies the collisionless Boltzmann (Vlasov) equation:

$$\frac{\partial f}{\partial t} + \frac{\partial \psi}{\partial y} \frac{\partial f}{\partial x} - \frac{\partial \psi}{\partial x} \frac{\partial f}{\partial y} = 0. \quad (10)$$

This equation has an infinite number of conserved quantities, which are known as the Casimir invariants. In particular, volumes occupied by different levels of the distribution function are the Casimir invariants of the Vlasov equation. This suggests that one can apply Lynden-Bell’s (LB’s) theory of collisionless relaxation to Euler hydrodynamics of 2D inviscid fluid.

II. LYNDEN-BELL THEORY

Lynden-Bell (LB) suggested that the equilibrium state resulting from collisionless relaxation should correspond to the maximum of Boltzmann entropy, under constraints that the Casimir invariants of the Vlasov dynamics be preserved [9]. In particular, volume occupied by different levels of the distribution function are Casimir invariants, as well as any functional of the distribution function. LB then suggested that in addition to the usual constraint of conservation of total energy and momentum, conservation of phase-space volume corresponding to different phase space levels of the initial distribution must be also taken into account. For an arbitrary initial flow, this requires an infinite number of Lagrange multipliers, which makes the solution of LB’s equations very difficult. Below we provide a stochastic technique that allows us to easily find LB’s equilibrium using a Monte Carlo (MC) approach.

According to LB’s idea, the initial continuous vortex distribution can be discretized in different levels. The phase space—which in the case of vortex dynamics is simply the configuration space (x, y) —is then divided into macrocells that in turn are subdivided into microcells. All the macroscopic observables are defined on the level of macrocells, while the incompressibility intrinsic to the Vlasov dynamics prevents more than one level from occupying a given microcell. This is schematically demonstrated in Fig. 1. During the evolution, the initial distribution function spreads over

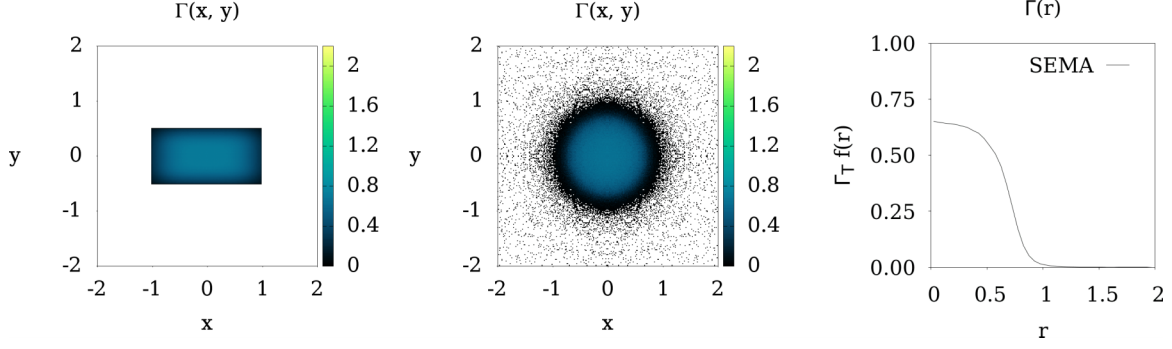


FIG. 3. Snapshots of the phase space obtained using the SEMA. The left panel shows the initial condition of a continuous distribution function, $f(x, y) = 0.7e^{-x^4 - 16y^4} \Theta(1.0 - |x|) \Theta(0.5 - |y|)$, normalized to unity. The central panel shows the steady state corresponding to LB equilibrium, while the right panel shows the radial distribution.

the phase space until a state of maximum disorder (entropy), consistent with all the conserved quantities, is reached.

To find the equilibrium distribution within LB theory, we start by discretizing the initial vortex distribution function $f(x, y)$ into the discrete function $\bar{f}(i, j)$ whose domain is a regular lattice that corresponds to the macrocells' centers. This rectangular lattice is built from the tensor product of two uniform grids of $(-L, L)$:

$$\{x_i = (i - 0.5)h_x - L, \quad i = 1, \dots, M, \quad h_x = 2L/M\}, \quad (11)$$

$$\{y_j = (j - 0.5)h_y - L, \quad j = 1, \dots, N, \quad h_y = 2L/N\}, \quad (12)$$

such that the coordinate (x, y) in the configuration space maps to the center node of the ij cell in the Eulerian mesh, that is, $f(x, y) \rightarrow \bar{f}(i, j)$, or \bar{f}_{ij} for short. Each of the lattice's cells contains ν microcells, for which the density of the microcell of index k is η_k , and the density at coordinate (i, j) is simply the arithmetic mean over all its microcells:

$$\bar{f}_{ij} = \frac{1}{\nu} \sum_{k=1}^{\nu} \eta_{ij,k}. \quad (13)$$

At the beginning, the density levels are set to a value identical to the distribution function in the corresponding coordinate, i.e., $\eta_{ij,k} = f(x_i, y_j) \forall k \in \{1, \dots, \nu\}$, so all the microcells within a macrocell (i, j) have exactly the same density level. The potential (stream function, ψ_{ij}), produced

by the density distribution function, \bar{f}_{ij} , is computed on an identical $M \times N$ Eulerian mesh (on the macrocells) using the discrete Poisson equation

$$(\Delta \psi)_{ij} = -2\pi \bar{f}_{ij},$$

$$(D_{xx}^2 \psi)_{ij} + (D_{yy}^2 \psi)_{ij} = -2\pi \frac{1}{\nu} \sum_{k=1}^{\nu} \eta_{ij,k}, \quad (14)$$

where the second central difference operator is denoted by

$$(D_{xx}^2 \psi)_{ij} \equiv \frac{\psi_{i+1,j} - 2\psi_{i,j} + \psi_{i-1,j}}{h_x^2} \quad \text{and} \quad (15)$$

$$(D_{yy}^2 \psi)_{ij} \equiv \frac{\psi_{i,j+1} - 2\psi_{i,j} + \psi_{i,j-1}}{h_y^2}, \quad (16)$$

with Dirichlet boundary conditions within a disk Ω of radius L , $\partial\Omega = 0$. The results shown in this paper were obtained using a square grid of dimensions M, N equal to 512, the number of microcells per macrocell $\nu = 32$, and the length of each macrocell is $h_x = h_y = 0.0039L$. The potential is computed with the aid of the successive-over relaxation iterative method [10]. The total energy and angular momentum of the initial distribution are, respectively,

$$E_0 = h_x h_y \frac{1}{2} \sum_{i,j} \bar{f}_{ij} \psi_{ij}, \quad (17)$$

$$L_0 = h_x h_y \sum_{i,j} \bar{f}_{ij} r_{ij}^2, \quad (18)$$

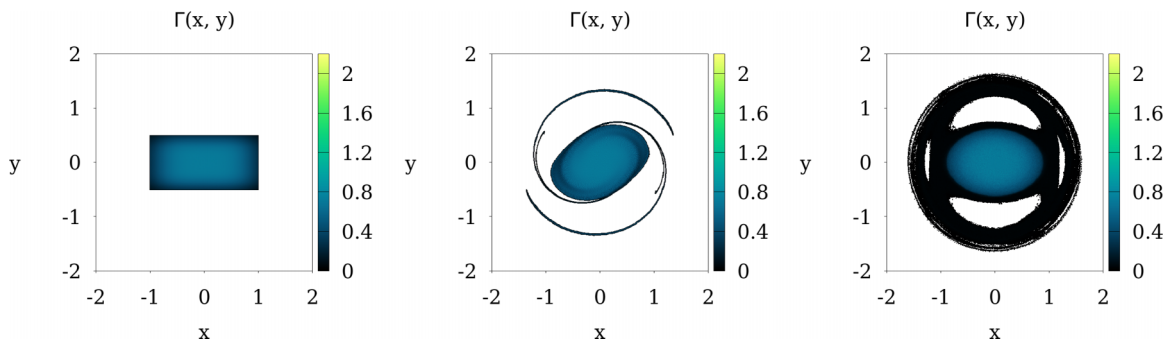


FIG. 4. Snapshots of the phase space obtained using MD simulation. The figures show the evolution of the initial condition of Fig. 3 (left panel). Note the rotation of the distribution function as it evolves. The vortices that are ejected from the core region move along the separatrix orbit, resulting in a steady state different from LB distribution.

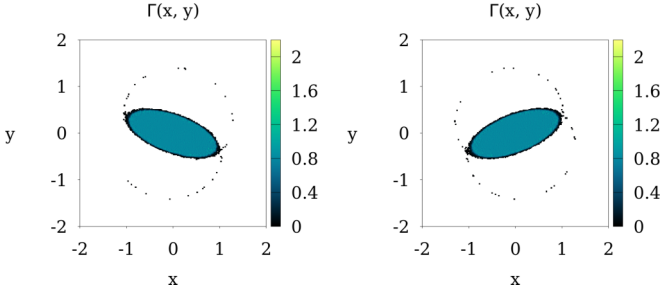


FIG. 5. Snapshots of the phase space obtained using MD simulation. The figures show the early stages of evolution of the initial condition $f(x, y) = (2.5/\pi) \Theta(1.0 - x^2 - 6.25y^2)$. Notice that even without linear instabilities, vortices are ejected and concentrate in the resonant region.

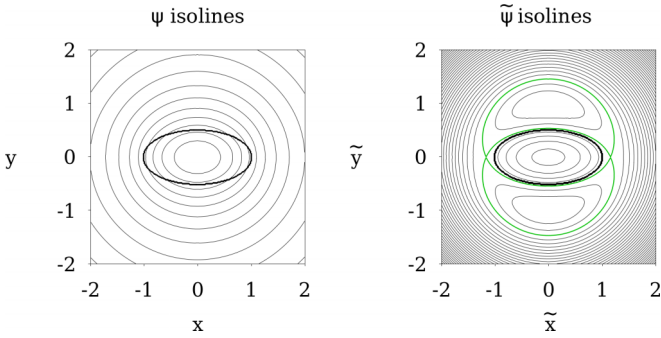


FIG. 6. Isolines of the potentials (thin lines) produced by a Kirchhoff’s vortex (thick lines): The left panel shows the potential in the laboratory reference frame, while the right panel shows the transformed potential in the rotating reference frame. The transformed potential exhibits a separatrix between high- and low-energy regions (green lines).

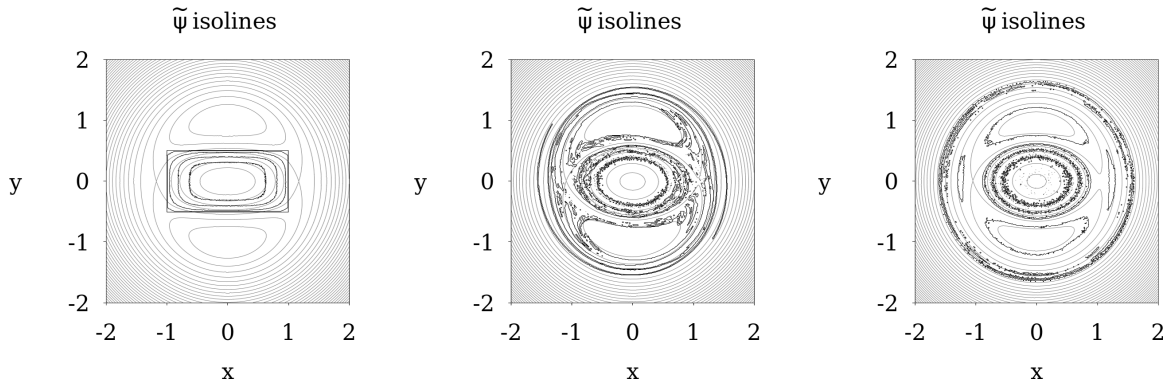


FIG. 7. Contour plots—in the rotating reference frame, with ω calculated using Eq. (32)—of the stream function (thin lines) and of isodensities (points) obtained using MD simulation and Eqs. (28). The panels correspond to the contour plots in Fig. 4. The final steady state (right panel) exhibits exact isopotentials, while the initial (left panel) and intermediary (central panel) states’ isopotential curves are approximate, since the distribution functions undergoes distortion as it rotates. One can see that vortices rearrange themselves by spreading along the equipotential lines.

and are conserved by the dynamics. To find the maximum entropy state, we developed a stochastic entropy maximization algorithm (SEMA) based on a canonical MC with two Lagrange multipliers α and β —the first to conserve the total angular momentum and the second the total energy inside the system. The basic steps of SEMA are the following:

- (1) Select two macrocells at random. The first macrocell is selected and then removed from a list containing all macrocells of the grid.
- (2) For each of the selected macrocells, select a microcell at random. If a microcell is empty, its density level is zero.
- (3) Compute the energy and angular momentum variation for the attempted exchange,

$$\delta E = (\eta_{A,1} - \eta_{B,2}) \times (\psi_A - \psi_B), \quad (19)$$

$$\delta L = (\eta_{A,1} - \eta_{B,2}) \times (r_A^2 - r_B^2), \quad (20)$$

where A and B refer to the macrocells containing microcells 1 and 2, respectively. r^2 is the square distance from the center to the macrocell and ψ is the stream function.

- (4) The acceptance probability for the exchange of density levels between the two microcells is given by the Metropolis algorithm,

$$e^{-\beta\delta E - \alpha\delta L} > P(X), \quad (21)$$

where $P(X)$ is a uniform random number between 0 and 1. Starting with an initial guess, the Lagrange multipliers β and α must be adjusted so the energy and angular momentum are conserved.

- (5) Perform steps 1 through 4 until all coordinates are chosen exactly one time. This will define a one Monte Carlo step (MCS). Then, reinitialize the list used in the first step.

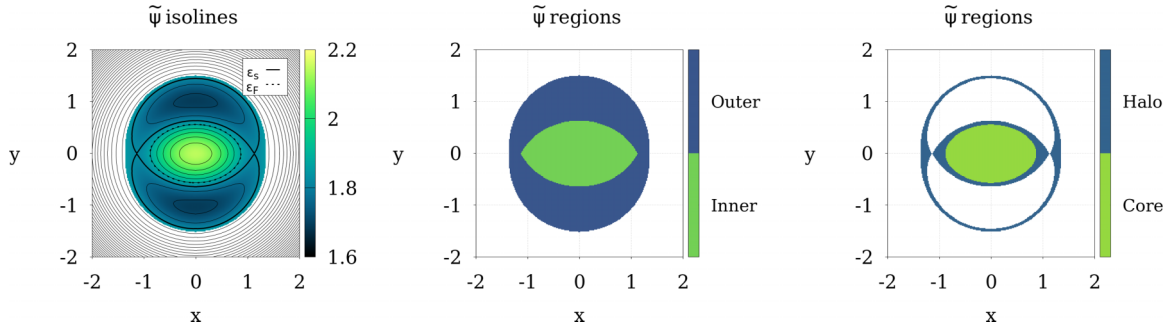


FIG. 8. Contour plot of the stream function and divisions of the phase space into distinct regions: The left panel shows isopotentials of the stream function, including the separatrix ϵ_s and the Fermi energy ϵ_F . The uncolored region marks all outer isopotentials with energy greater than the halo energy ϵ_h —the separatrix of the initial distribution; the central panel shows the division of the phase space into inner and outer regions. The interface between them is delimited by the separatrix, while the outer region is also bounded externally by ϵ_h ; the right panel shows further division into core and halo regions. The core is defined as the inner region whose potential is above ϵ_F , while the halo is defined as the inner region whose potential is below ϵ_F plus the outer region whose potential is between ϵ_h and ϵ_s .

(6) After each MCS, the values of \bar{f} and ψ are updated. The Lagrange multipliers are updated as

$$\beta^{(\text{new})} = \beta^{(\text{old})} + \sigma_E(E - E_0)/E_0, \quad (22)$$

$$\alpha^{(\text{new})} = \alpha^{(\text{old})} + \sigma_L(L - L_0)/L_0, \quad (23)$$

where E and L are, respectively, the energy and angular momentum of the current iteration and E_0 and L_0 are the conserved values of these quantities. The parameter σ controls the speed of updates. The updates will stop when both energy and angular momentum converge to the target values E_0 and L_0 .

For an initial-one level water-bag distribution of vortices, the LB distribution corresponding to the maximum entropy state can be calculated explicitly and is given by

$$f_{\text{LB}}(\mathbf{r}) = \frac{\eta}{1 + e^{\eta(\beta\psi(\mathbf{r}) + \alpha r^2 - \mu)}}, \quad (24)$$

where η is the level density in the initial distribution, see Fig. 2 (left panel). Combining this with the Poisson equation for the stream function ψ and taking into account the conservation of energy and angular momentum allows us to uniquely determine the parameters α , β and the stream function $\psi(r)$. The radial vortex density distribution is plotted in Fig. 2 (right panel), where we have also plotted the data points obtained using SEMA. We see that the results of SEMA are in excellent agreement with the numerical solution of LB theory. In Fig. 2 (center panel), we also show the equilibrium density distribution of vortices over the configuration space calculated using SEMA.

TABLE I. Definition and update rules of pertinent parameters for the phase space division into active and inactive regions. At the beginning, $\epsilon_s = \epsilon_h$ by definition, while $\epsilon_F = \epsilon_s$ as the first guess.

	Initial value	Update rule
ϵ_h	separatrix of initial condition	$\epsilon_h = \tilde{\psi}(x=0, y=y_m)$
ϵ_s	separatrix of initial condition	recomputed as the separatrix of current distribution
ϵ_F	separatrix of initial condition	updated according to Eq. (33)

The advantage of SEMA is that it automatically accounts for different density levels of the initial distribution, while if we attempt direct entropy maximization these must be included as an infinite set of Lagrange multipliers. For example, in Fig. 3 we study relaxation of the initial distribution $f(x, y) \propto \exp(-x^4 - 16y^4)$. The equilibrium density distribution calculated using SEMA is shown in Fig. 3 (center panel), while the radial density distribution function is shown in Fig. 3 (right panel).

Although theoretically very appealing, comparing the predictions of LB theory with molecular dynamics (MD) simulation based on the equations of motion, Eqs. (9), we see that the final state to which the system evolves is very different than what is predicted by the LB theory. The MD simulations were performed with $2^{23} \equiv 8\,388\,608$ vortices. To minimize collisional effects, the density distribution function was computed using a particle-in-cell technique [11] on a grid identical to that used by the statistical approaches. The state of the system was advanced using a fifth-order Runge-Kutta algorithm with an error of order 10^{-6} . Instead of a circularly symmetric stationary solution predicted by LB and observed in Figs. 2 and 3, we find a very complicated noncircular core-halo structure undergoing rotation with constant angular velocity ω [2], see Fig. 4. Clearly, another approach must be taken to understand the complex relaxation observed in 2D Euler fluids. We will do this in the next section by combining the theory of core-halo with a SEMA-like algorithm.

III. THE CORE-HALO MODEL APPROACH

The core-halo theory was introduced to account for the relaxation of an elliptical Kirchhoff vortex patch. It is well-known that a highly eccentric elliptical vortex patch is susceptible to linear instabilities [12,13], however, even low-eccentricity elliptical Kirchhoff vortices are susceptible to nonlinear instabilities in which the vortices close to the border enter in resonance with the rotation of the patch and are ejected from the macro vortex [2], see Fig. 5.

Since the Hamiltonian (Kirchhoff function) depends only on x and y coordinates, the vortices that are ejected end up with lower energy than vortices that are inside the core region. The process of evaporative heating results in the

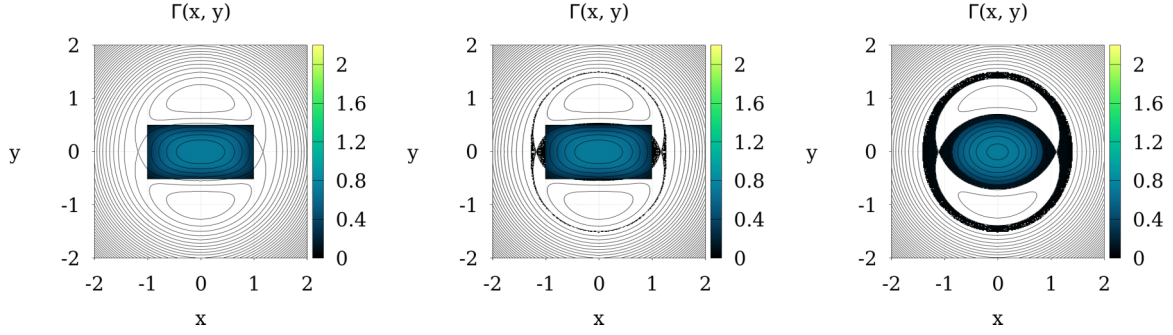


FIG. 9. Subsequent stages of SCHA corresponding to the evolution of the distribution function shown in Fig. 4 with the contour plot of its potential overlaid over the phase-space snapshots. Note that the vortices move from *inactive* regions according to the established criteria for core and halo regions.

reorganization of the core region and formation of a core-halo structure. The situation becomes clearer if we transform into the reference frame that rotates together with the vortex patch: $(x, y) \rightarrow (\tilde{x}, \tilde{y})$,

$$\tilde{x} = +x \cos(\omega t) + y \sin(\omega t), \tag{25}$$

$$\tilde{y} = -x \sin(\omega t) + y \cos(\omega t), \tag{26}$$

with angular velocity ω of the elliptical Kirchhoff vortex. The canonical coordinate transformation can be described by the generating function,

$$\mathcal{F}(x, \tilde{y}) = \frac{x\tilde{y}}{\cos(\omega t)} + \frac{x^2 + \tilde{y}^2}{2} \tan(\omega t), \tag{27}$$

such that $\tilde{x} = \partial\mathcal{F}/\partial\tilde{y}$ and $y = \partial\mathcal{F}/\partial x$. Since the generating function has an explicit time dependence, the stream function in the rotating reference frame will be

$$\tilde{\psi}(\tilde{x}, \tilde{y}) = \psi(\tilde{x}, \tilde{y}) + \frac{\partial\mathcal{F}}{\partial t}, \quad \frac{\partial\mathcal{F}}{\partial t} = \frac{\omega}{2}(x^2 + \tilde{y}^2). \tag{28}$$

In Fig. 6, we plot the equipotential curves corresponding to the stream function in the laboratory and in the rotating reference frame. We see that while in the laboratory frame the surface of the ellipse is not an equipotential, in a rotating reference frame with a specific value of ω the surface of the ellipse becomes an equipotential. This means that it is possible to write the distribution function in a way that the depen-

dence on coordinates appears only through $\tilde{\psi}(x, y)$, where to simplify the notation we have removed the tilde over x and y . This implies that rotating the Kirchhoff elliptical vortex is a stationary solution (in the rotating reference frame) of the Vlasov equation. In the thermodynamic limit, the Kirchhoff vortex would rotate forever. In practice, however, it is susceptible to small perturbations which can lead to linear and nonlinear instabilities [13–16]. The perturbed vortices are caught by the separatrix isopotential trajectory, resulting in vortex evaporation and halo formation, see Fig. 6.

The separatrix trajectory captures vortices that are close to the border of the ellipse and moves them away to the low-energy regions of phase space, forming a halo, while other vortices compensate for this by moving into high-energy regions inside the core. This results in the population inversion in the core region. This process can continue until all the high-energy levels inside the core are fully occupied up to the Fermi energy, producing a fully degenerate cold core. In the present case, we think of cold as $T \rightarrow 0^-$, which is consistent with Onsager’s idea of negative temperature. The final state is a characteristic core-halo structure with a population-inverted core region.

In the laboratory frame, formation of the halo follows a filamentation process, as can be seen in Fig. 4. As the original vortex patch undergoes relaxation, vortices are captured by the resonance and follow the separatrix orbit, which takes them away from the core region. Evaporation perturbs the rotation

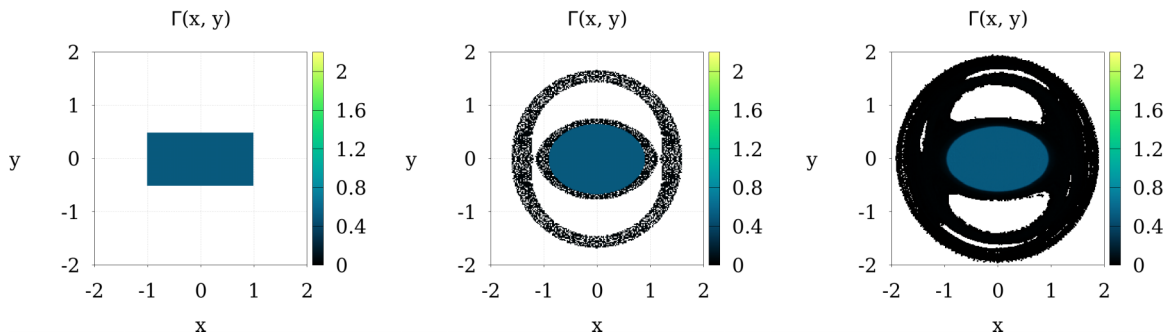


FIG. 10. Snapshots of the phase space obtained using SCHA and MD simulation. The left panel shows the initial condition of a one-level rectangular distribution function, $f(x, y) = 0.5 \Theta(1.0 - |x|) \Theta(0.5 - |y|)$, normalized to unity. The central panel shows the steady state obtained using SCHA, while the right panel shows the steady state obtained using MD simulation. The MD simulation has a halo that extends farther than predicted by the theory.

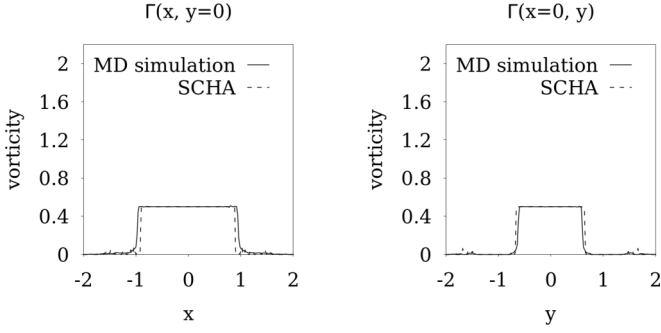


FIG. 11. Comparison of the density distribution over the x and y axes of the steady states obtained using SCHA and MD simulations. These correspond to the steady states shown in Fig. 10.

of the core, affecting the resonant orbit (separatrix), which moves inward toward the core. Since the ejected vortices go to the low-energy region of the phase space, the vortices in the core rearrange themselves so the total energy remains conserved. However, because of the incompressibility constraint imposed by Vlasov dynamics, the process cannot continue indefinitely, and at some point the core will become frozen—all the free energy liberated by the evaporated vortices will result in a fully degenerate cold core in which all the highest energy states up to the Fermi energy are occupied. At this point, the process of evaporative heating must come to an end. In practice, one often sees incomplete relaxation, in which the core does not reach a fully degenerate frozen state.

To solve the core-halo model, we must self-consistently calculate the stream function produced by the particle distribution with a core-halo structure. Inside the core, the temperature is $T \rightarrow 0^-$, which requires the occupation of energy levels inside the stream function to follow a hierarchical structure, where the higher density levels will be closer to the center of the core than the low density levels. Simultaneously with this, there is a process of vortex evaporation that leads to formation of a halo. In principle, it is possible to write the equations that will allow us to calculate the core-halo structure self-consistently, accounting for the conservation of the total energy and momentum, as well as the volume occupied by all the density levels in the initial distribution function. In practice, however, it is easier to solve the core-halo theory using a stochastic algorithm, similar to what we did for LB theory.

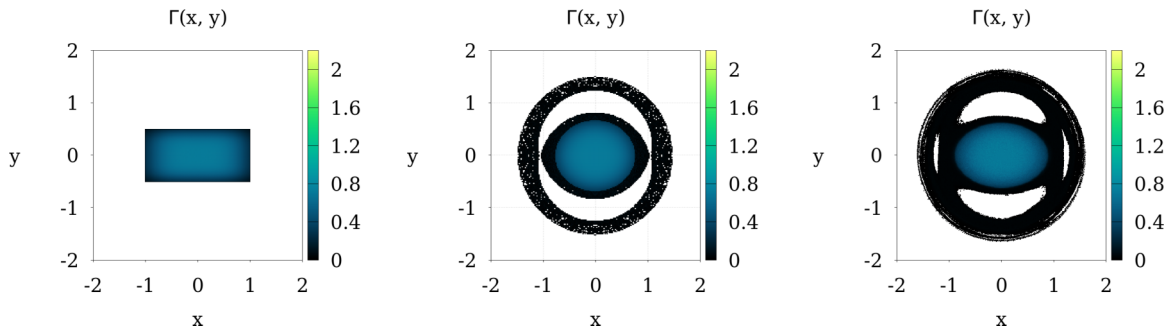


FIG. 12. Snapshots of the phase space obtained using SCHA and MD simulation. The left panel shows the initial condition of a continuous rectangular distribution function, $f(x, y) = 0.7 e^{-x^4 - 16y^4} \Theta(1.0 - |x|) \Theta(0.5 - |y|)$, normalized to unity. The central panel shows the steady state obtained using SCHA, while the right panel shows the steady state obtained using MD simulation.

We will call this stochastic core-halo algorithm (SCHA). The algorithm is based on the following subdivision of the phase space: In the rotating reference frame, the configuration space is divided into two active regions, namely, core and halo, in which density levels are allowed to remain. The separatrix then divides the configuration space into a high-energy inner region and a low-energy outer region. The core corresponds to an inner, maximally packed, cold region bounded by a Fermi energy ϵ_F , and the halo corresponds to a low density nonuniform region extending from the inner region to the outer region, where it is bounded by the halo energy ϵ_h —the halo energy is defined as the value of the isopotential corresponding to the maximum y_m of the separatrix of the initial distribution, $\epsilon_h = \tilde{\psi}(x=0, y=y_m)$. The angular velocity of the vortex patch (which is also the angular velocity of the rotating reference frame) is calculated using the inertia tensor of the distribution:

$$\mathbf{I} = \begin{bmatrix} \langle x^2 \rangle & -\langle xy \rangle \\ -\langle xy \rangle & \langle y^2 \rangle \end{bmatrix}. \quad (29)$$

The angle, θ , between the x axis and the major principal axis of the distribution can be found using the arctan function and the components of one of the eigenvectors computed from the inertia matrix, Eq. (29):

$$\theta = \arctan \left(\frac{2\langle xy \rangle}{\langle y^2 \rangle - \langle x^2 \rangle - \sqrt{4\langle xy \rangle^2 + (\langle x^2 \rangle - \langle y^2 \rangle)^2}} \right). \quad (30)$$

The instantaneous angular velocity can be calculated as the time derivative of θ . Assuming that the distribution is axisymmetric and that at the time of measurement the principal axis coincides with x and y axis, so $\langle xy \rangle \rightarrow 0$, we obtain

$$\omega = \frac{d\theta}{dt} = -\frac{\langle \dot{xy} \rangle}{\langle x^2 \rangle - \langle y^2 \rangle} = -\frac{\langle x\dot{y} + y\dot{x} \rangle}{\langle x^2 \rangle - \langle y^2 \rangle}. \quad (31)$$

The Eulerian mesh or discretized version of the above equation can be written as

$$\omega \equiv -\frac{\sum_{i=1}^M \sum_{j=1}^N \bar{f}_{ij} (x_i \dot{y}_j + y_j \dot{x}_i)}{\sum_{i=1}^M \sum_{j=1}^N \bar{f}_{ij} (x_i^2 - y_j^2)}, \quad (32)$$

where M and N are the dimensions of the Eulerian mesh.

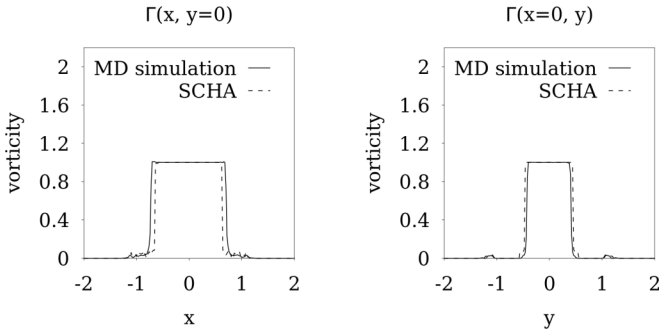


FIG. 13. Comparison of the density distribution over the x and y axes of the steady states obtained using SCHA and MD simulations. These correspond to the steady states shown in Fig. 12.

Unlike for the Kirchhoff elliptical vortex patch, the steady-state angular velocity of an arbitrary initial distribution is not known *a priori*. For example, the isopotential lines shown in Fig. 7 (left and center panels) are only approximations, since in the early stages of evolution the rectangular vortex patch is undergoing distortion and does not rotate as a rigid body. The isopotentials were obtained using Eqs. (28) with angular velocity ω computed from the actual particle distribution functions obtained from MD simulation using Eq. (32). We see that the point vortices in the MD simulation clearly follow the trajectories described by the isopotential lines. Figure 7 (right panel) shows that even after the dynamics has long stopped in the core region, the halo continues to evolve through the process of filamentation. However, since the halo is so tenuous and has a *quasicircular* symmetry it does not contribute significantly to the resulting angular velocity.

Following the structure of isopotentials, we see that while the core exists only in the inner region, the halo extends between the inner and outer regions. This is illustrated in Fig. 8. The core is defined as the inner region whose potential is above the Fermi energy ε_F , which will be calculated self-consistently as will be described below. The halo region is defined as the inner region whose potential is below ε_F plus the outer region whose potential is between the halo energy ε_h and the separatrix region ε_s , see Fig. 8 (right panel). Core and halo belong to *active* regions, namely, the regions for which exchange of density levels is allowed. Density levels

can also be found in the inactive regions—outside the core and halo—due to the initial distribution or due to previously active regions becoming inactive as the separatrix moves inward. Therefore, transfer from inactive to active regions is allowed, but not vice versa.

The rules of SCHA are very simple. Steps 1 to 3 and step 5 of SCHA are identical to those of the SEMA algorithm, while steps 4 and 6 are modified as follows:

(4) Evaluate the acceptance of exchange of density levels between the two microcells: The variation in energy must be positive if the exchange involves a microcell within the core region. Random exchange of levels within the halo region is allowed. Additionally, the variation in angular momentum must be kept very small, on the order of a single exchange, i.e., with the exception of the first exchange, all exchanges must compensate for the resulting difference, which means that if the previous movement resulted in an excess of angular momentum, only exchanges that decrease angular momentum are accepted, and vice versa. This means that—apart from small fluctuations—the angular momentum is always conserved.

(6) After one MCS, the stream function and angular velocity are recalculated. Finally, the Fermi energy is updated,

$$\varepsilon_F^{(\text{new})} = \varepsilon_F^{(\text{old})} + \sigma_E(E - E_0)/E_0, \quad (33)$$

where E is the current iteration energy and E_0 is the energy of the initial distribution that must be conserved.

In the present paper, we used $\sigma_E = 1$ for the speed of updates and ε_F is initially set to ε_s , so the core region is defined as the inner region. In SCHA, the Fermi energy acts as a Lagrange multiplier which is adjusted so the total energy inside the system is conserved—when the resulting energy E is larger than E_0 , the Fermi energy increases, making the core region smaller, so the vortices that were part of the core are scattered into the halo region and the total energy decreases. If the resulting energy E is smaller than E_0 , then the Fermi energy decreases, making the core region larger and allowing more vortices to migrate into the central region, increasing the energy. The updates in Eq. (33) will end when the distribution converges to the final stationary state with energy $E = E_0$. Note that the total energy is computed in the laboratory frame. This is necessary because the rotational velocity changes with each iteration until a stationary state is reached. The initial

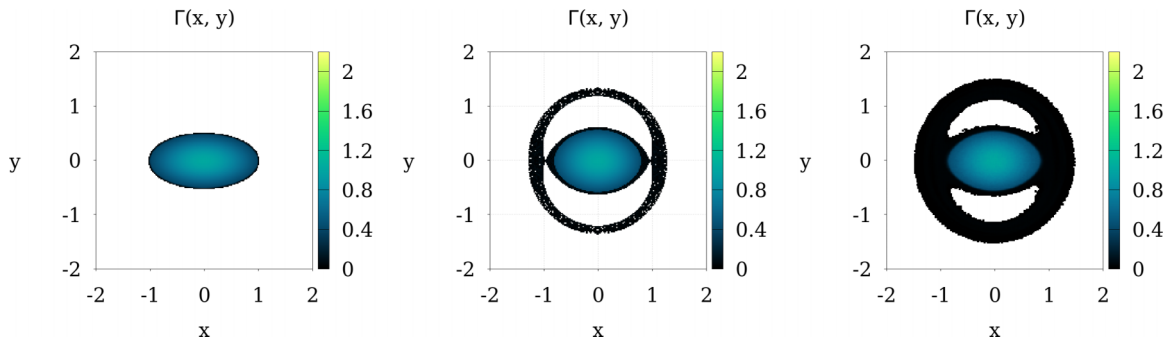


FIG. 14. Snapshots of the phase space obtained using SCHA and MD simulations. The left panel shows the initial condition of a continuous distribution function, $f(x, y) = 1.0 e^{-x^2-4y^2} \Theta(1.0 - x^2 - 4y^2)$, normalized to unity. The central panel shows the steady state obtained using SCHA, while the right panel shows the steady state obtained using MD simulation.

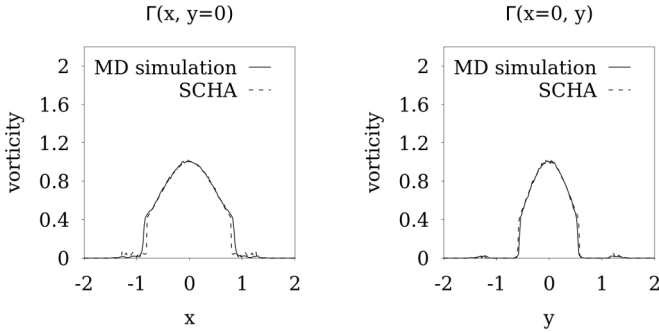


FIG. 15. Comparison of the density distribution over the x and y axes of the steady states obtained using SCHA and MD simulations. These correspond to the steady states shown in Fig. 14.

value and the update rules of ϵ_h , ϵ_s , and ϵ_F are shown in Table I.

The different stages of SCHA are illustrated in Fig. 9. It shows the early stages of the distribution function overlaid by the isopotential levels of the stream function as the calculation progresses. The vortices move from *inactive* regions into the core and the halo regions, according to the established rules.

Starting from a continuous vortex distribution, SCHA converges to a highly nontrivial distribution function that rotates in the laboratory frame with a constant angular velocity $\omega = 0.85$ and has a high-density elliptical core surrounded by a low-density halo, see Fig. 9. The final steady state is shown in Fig. 12 (center panel). In MD simulations, the rotational velocity is found to be $\omega = 0.95$. This happens because the expression for the angular velocity—as per Eq. (32)—depends on the distribution of vortices and the result of the MD is somewhat more elliptical than the one calculated by the statistical method, compare Fig. 12 center and right panels. In Figs. 10–19, we consider more complex continuous initial distributions and also compare the resulting stationary (in the rotating frame) density profiles with the results of MD simulations.

One flaw of the core-halo theory is that the maximum extent of the halo is calculated from the separatrix of the initial vortex distribution function. If such a distribution function is linearly unstable, which is the case for high aspect ratios, the resulting instability can expel vortices farther than the extent

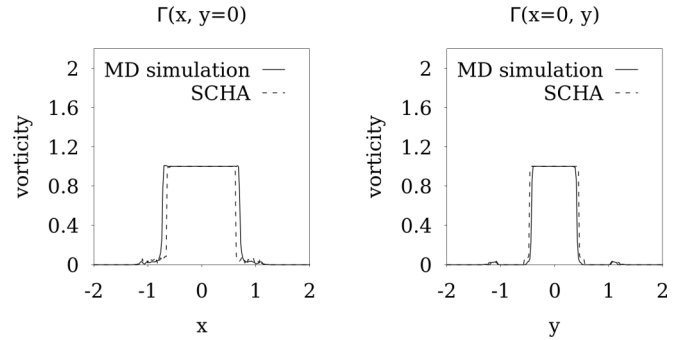


FIG. 17. Comparison of the vortex density distribution along the x and y axes in the steady state predicted using SCHA and compared with MD simulations. These correspond to the steady state shown in Fig. 16.

of the separatrix [16]. Figures 10, 12, 14, and 16 show the stationary solutions (in rotating frame) compared with MD simulations for various initial distributions. One can see that for these initial distributions, the halos extend farther than what is predicted by the theory. Nevertheless, since the halo density is so small, this has only a very minor effect on the density distribution and the shape of the core region, which are very accurately described by the core-halo theory. To obtain a more quantitative comparison of theory with simulations, Figs. 11, 13, 15, and 17 present the vortex density distributions along the principal axis, showing that the theory quantitatively accounts for the density distribution within the core and semi-quantitatively inside the halo. What is even more impressive is that theory predicts that one-level rectangular distribution with the aspect ratio larger than ~ 6.3 will break up into two identical distorted elliptical vortex patches of complex shape surrounded by a halo which will rotate around their center of mass. This is quantitatively verified using MD simulations, which shows that the breakup into two identical vortex patches occurs for an aspect ratio of ~ 6.1 or greater. Figures 18 and 19 compare the steady state obtained from SCHA and MD simulation for an aspect ratio of 6.5, showing excellent agreement. Furthermore, the theory predicts that the two-blob core will rotate around its center of mass with $\omega = 0.944$, while MD finds $\omega = 0.939$.

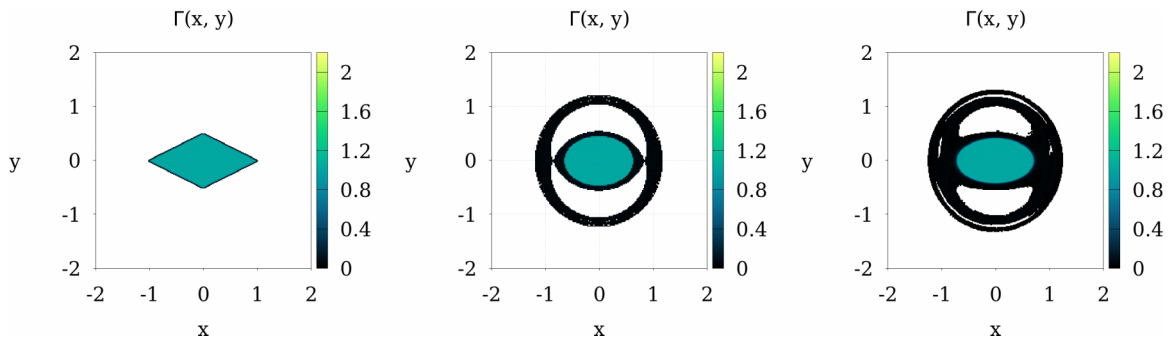


FIG. 16. Snapshots of the phase space obtained using SCHA and MD simulations. The left panel shows the initial condition of a one-level rhombic distribution function, $f(x, y) = \Theta(1.0 - |x| - 2|y|)$, normalized to unity. The central panel shows the steady state obtained using SCHA, while the right panel shows the steady state obtained using MD simulation. As in the other simulations, the MD simulation exhibits a thicker halo, but the core predicted by SCHA is very similar to the core observed in the MD simulation.

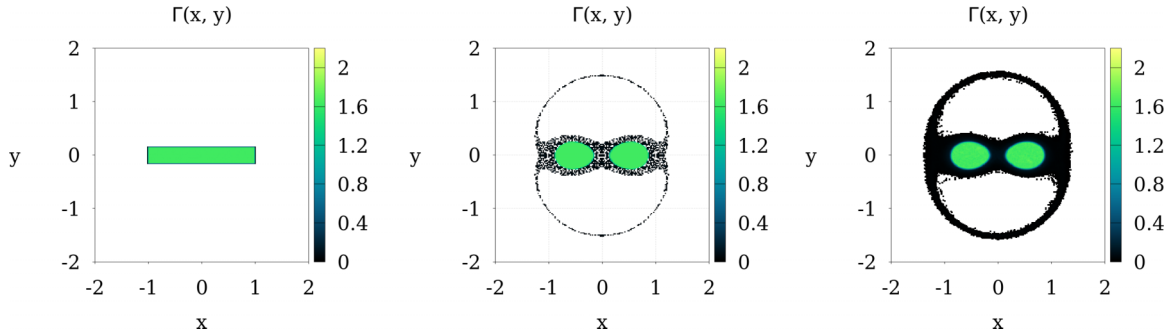


FIG. 18. Snapshots of the phase space obtained using SCHA and MD simulations. The left panel shows the initial condition of a one-level rectangular distribution function, $f(x, y) = 1.625 \Theta(1.0 - |x|) \Theta(1/6.5 - |y|)$, normalized to unity. The central panel shows the steady state obtained using SCHA, while the right panel shows the steady state obtained using MD simulation. As in the other simulations, the MD simulation exhibits a thicker halo.

IV. CONCLUSION

We have used Kirchhoff’s vortex formalism to explore stationary solutions of 2D Euler fluid equations. The vortex dynamics obeys Hamilton’s equations of motion with x and y coordinates of vortex position forming a conjugate pair. A state of fluid can, therefore, be expressed in terms of infinite number of infinitesimal vortices.

The Hamiltonian structure of the vortex dynamics naturally draws an analogy with short-range interacting particles systems. Specifically, we know that the equilibrium state to which a many-body system—such as a gas or an electrolyte solution or a colloidal suspension—will evolve from an arbitrary initial distribution can be calculated using MD simulations. On the other hand, we know that this is not necessary, since Boltzmann-Gibbs statistical mechanics allows us to predict the final thermodynamic equilibrium without performing explicit MD simulations. Based on this, we can calculate the final distribution functions inside a liquid, solid, electrolyte, etc. using equilibrium statistical mechanics. In practice, it is often impossible to calculate the partition function except for very simple systems. A practical solution is to use MC simulations to obtain the equilibrium state of a system. MC dynamics has nothing to do with the dynamics

of MD simulations, which relies on solution of Newton’s equations of motion. It is just a statistical tool to numerically perform entropy maximization. The difficulty is that for systems with long-range interactions—such as vortices in Euler fluid, gravitational systems, and magnetically confined plasmas—one cannot use Boltzmann-Gibbs statistical mechanics. These systems do not evolve to thermodynamic equilibrium but become trapped in nonequilibrium steady states [8].

If the vortex dynamics would be mixing, the final equilibrium state of the fluid would correspond to the maximum of the Boltzmann entropy, with the constraint that all the Casimir invariants of the fluid are conserved. This is the basic assumption of LB’s theory of collisionless relaxation. In this paper, we have presented a stochastic method that allows us to find the maximum entropy state of the fluid starting from an arbitrary initial distribution of vortices. We then compared the predicted stationary distributions for various initial conditions with the results of MD simulations and demonstrated that the final state to which the fluid evolves is indeed very different from that of maximum entropy. This indicates that the mixing assumption is not valid. We then presented a core-halo theory which allows us to semiquantitatively predict the final state to which the fluid will relax. In practice, the core-halo equations are very difficult to solve except for very simple water-bag initial distributions. In the present paper, we showed how these equations can be solved using a stochastic method similar to MC simulations for systems with short-range interactions. We then applied the theory to predict the final stationary state to which various vortex patches will evolve. We find that, in general, the vortex distributions are only stationary in a rotating reference frame, while in the laboratory frame they rotate with a constant angular velocity, which the theory allows us to predict explicitly. If the starting vortex distribution has a large aspect ratio, we find that in the stationary state it will split into two distorted elliptical vortex patches which rotate around their center of mass and are surrounded by a tenuous halo. The theory allows us to accurately predict the bifurcation point and the final stationary vortex distribution. All the theoretical predictions were compared with the explicit MD simulations and were found to be in good agreement. In future work, we intend to apply the

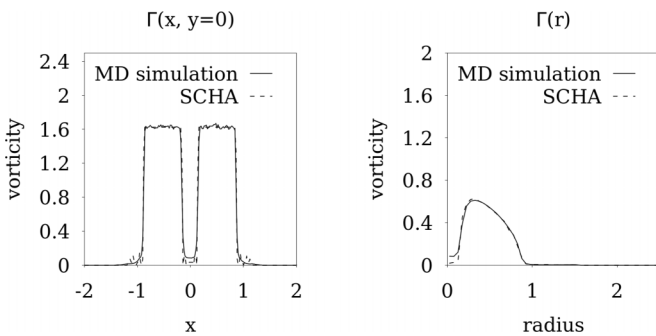


FIG. 19. Comparison of the density distribution over the x axis and radial distribution of the steady states obtained using SCHA and MD simulations. These correspond to the steady states shown in Fig. 18. The radial distribution is defined as $\Gamma(r) = (2\pi)^{-1} \int_0^{2\pi} \Gamma(r, \theta) d\theta$.

theory developed here to predict the stationary flows that result from Kelvin-Helmholtz instabilities of sheared 2D Euler fluid flows.

ACKNOWLEDGMENT

This work was supported by CAPES, CNPq, and INCT-FCx.

-
- [1] L. Onsager, Statistical hydrodynamics, *Nuovo. Cim.* **6**, 279 (1949).
 - [2] R. Pakter and Y. Levin, Nonequilibrium Statistical Mechanics of Two-Dimensional Vortices, *Phys. Rev. Lett.* **121**, 020602 (2018).
 - [3] L. M. Polvani and G. R. Flierl, Generalized Kirchhoff vortices, *Phys. Fluids* **29**, 2376 (1986).
 - [4] C. Marchioro and M. Pulvirenti, *Mathematical Theory of Incompressible Nonviscous Fluids* (Springer, New York, 1994).
 - [5] G. L. Eyink and K. R. Sreenivasan, Onsager and the theory of hydrodynamic turbulence, *Rev. Mod. Phys.* **78**, 87 (2006).
 - [6] A. Campa, T. Dauxois, and S. Ruffo, Statistical mechanics and dynamics of solvable models with long-range interactions, *Phys. Rep.* **480**, 57 (2009).
 - [7] A. Campa, T. Dauxois, D. Fanelli, and S. Ruffo, *Physics of Long-Range Interacting Systems* (Oxford University Press, Oxford, 2014).
 - [8] Y. Levin, R. Pakter, F. B. Rizzato, T. N. Teles, and F. P. C. Benetti, Nonequilibrium statistical mechanics of systems with long-range interactions, *Phys. Rep.* **535**, 1 (2014).
 - [9] D. Lynden-Bell, Statistical mechanics of violent relaxation in stellar systems, *Mon. Not. R. Astron. Soc.* **136**, 101 (1967).
 - [10] G. W. S, Templates for the solution of linear systems: Building blocks for iterative methods, *Math. Comput.* **64**, 1349 (1995).
 - [11] Yu. N. Grigoryev, V. A. Vshivkov, and M. P. Fedoruk, Iterative methods, *Numerical "Particle-in-Cell" Methods*, 1st ed., Theory and Applications (VSP, BV, Utrecht, Netherlands, 2002), Chap. 2.
 - [12] A. E. H. Love, On the stability of certain vortex motions, *Proc. London Math. Soc.* **s1-25**, 18 (1893).
 - [13] J. Burbea and M. Landau, The kelvin waves in vortex dynamics and their stability, *J. Comput. Phys.* **45**, 127 (1982).
 - [14] Sir W. Thomson, XXIV. Vibrations of a columnar vortex, *London Edinburgh Philos. Mag. J. Sci.* **10**, 155 (1880).
 - [15] T. B. Mitchell and L. F. Rossi, The evolution of Kirchhoff elliptic vortices, *Phys. Fluids* **20**, 054103 (2008).
 - [16] C. A. Fracassi Farias, R. Pakter, and Y. Levin, Linear and non-linear instabilities of Kirchhoff's elliptical vortices, *J. Stat. Mech.: Theory Exp.* (2020) 083205.